INTERNATIONAL JOURNAL FOR NUMERICAL METHODS IN FLUIDS, VOL. 15, 99–124 (1992)

NAVIER–STOKES COMPUTATIONS OF HORSESHOE VORTEX FLOWS

G. B. DENG AND J. PIQUET
CFD Group, LHN-URA 1217 CNRS, ECN, Nantes, France

SUMMARY

The computation of the incompressible three-dimensional turbulent viscous flow about an aerofoil/flat plate junction is investigated. An iterative, fully decoupled technique is applied to the Reynolds-averaged Navier–Stokes equations (RANSEs) written in a non-orthogonal curvilinear body-fitted co-ordinate system. The results of the computations are compared with well-documented experiments.

KEY WORDS Wing–body junction Horseshoe vortex flow Numerical solution Navier–Stokes equations Viscous–inviscid interaction

1. INTRODUCTION

The junction between a body and an appendage is a simple geometric configuration with a complex turbulent flow. Such configurations are found in many areas of fluid engineering such as wing–fuselage geometries, appendage–hull junctions of ships or submarines, blade–hub intersections on propellers, blade–end wall junctions of turbomachinery, high-rise buildings and bridge piers in rivers. The most important feature of the flow past such junctions is undoubtedly the horseshoe vortex system and the associated secondary flow which affects the drag, lift and heat transfer. A simplified description of this problem is considered here, namely aerofoil–flat plate junction flow. The considered aerofoil shape is a modified NACA 0020 with the nose section replaced by a 3:2 ellipse in order to make the vortex system more intense and to simplify the measurement task. Also, this wing shape, used in References 1 and 2, is more realistic than infinite chord wings, investigated for instance in Reference 3, which differ in the shape of the leading edge.

While junction flows have promoted a great deal of experimental work, numerical solutions of the flow have received relatively little attention owing to the complexity of the flow field and to the occurrence of large regions of reversed flow which forbids the use of parabolic methods starting from upstream. The first Navier–Stokes computations can be credited to Briley and McDonald,[4] who used a linearized block implicit scheme with an ADI-type splitting in order to solve at low Mach numbers the compressible Navier–Stokes equations for a laminar horseshoe root vortex created by the intersection of an elliptic strut and a flat plate (see also Reference 5). Most of the other solutions are focused on high-Mach-number compressible flows on wing–fuselage interactions and use a Baldwin–Lomax[6] turbulence model (see e.g. Reference 7). For low-speed incompressible flows a very few contributions have dealt with this problem. Burke[8] has used the so-called INS3D flow solver[9] which is based on the artificial compressibility method and uses the Baldwin–Lomax model. Similar computations with a fourth-order explicit Runge–Kutta scheme and fourth-order explicit artificial dissipation have been performed in Reference 10. Owing to the severe CFL restriction inherent to explicit time marching, acceleration

0271–2091/92/130099–26$18.00

Received April 1991
Revised November 1991

towards the steady state uses local time stepping and implicit residual smoothing through an approximate factorization technique. However, convergence difficulties linked to high cell aspect ratios made it necessary to introduce several improvements in the definition of the artificial dissipation, which was made self-adjusting to the flow parameters, and in the time-stepping procedure. Also, a multigrid technique was implemented, although the generated solution indicated signs of heavy dissipation.[11] Some extensive calculations using a collocative grid with a finite analytic method are presented in Reference 12. The method, apparently fast, uses a two-equation K–ε turbulence model, except close to the wall where the ε-equation is bypassed by means of the one-equation model.[13] In References 14 and 15 numerical results are presented with a method similar to that of Reference 12, although it differed from Reference 12 mainly in the hybrid-type numerical scheme and the turbulence model used.

Owing to the existence of very important experimental databases,[1,2] this geometry offers an opportunity to compare the numerical outputs of the computational method with experimental results involving massive separation and hence allows the validation of the numerical method on a case close to 'real life' situations. Apart from validation, the aim of the present work is to investigate the flow in more detail and to shed some light on significant aspects of the physics of the viscous–inviscid interaction. Such efforts are a prerequisite before more complex geometries involving one order of magnitude more points and computational time can be safely investigated.

2. THE EQUATIONS

We consider the equations of motion for incompressible flows. The exact RANSEs of continuity and momentum of the mean flow in dimensionless form are given by

$$\operatorname{div}\mathbf{U}=0, \tag{1}$$

$$\frac{\partial \mathbf{U}}{\partial t}+\nabla\cdot\mathbf{U}\mathbf{U}+\nabla p+\nabla\cdot\overline{\mathbf{u}\mathbf{u}}=\frac{1}{Re}\nabla^2\mathbf{U}, \tag{2}$$

where $\mathbf{U}$, p and $\overline{\mathbf{uu}}$ are the velocity vector, the pressure and the Reynolds stress tensor respectively. The resulting turbulent closure problem is solved by means of an algebraic viscosity model in which the Reynolds stress is linearly related to the mean rate-of-strain tensor through an isotropic eddy viscosity as follows:

$$\overline{\mathbf{uu}}=\tfrac{2}{3}k\,\mathbf{1}-\nu_{\mathrm{T}}(\nabla\mathbf{U}+\nabla^{\mathrm{T}}\mathbf{U}). \tag{3}$$

The standard Baldwin–Lomax model[6] is used. Close to the root the length scale is simply taken as the minimum distance n to one of the two walls. This model has been selected because of its simplicity. Also, it avoids discontinuities of the eddy viscosity ν_{T} close to the leading edge of the aerofoil, while avoiding transition problems which must be dealt with if transport models for turbulent quantities are used. As a consequence, k in (3) is neglected with respect to pressure.

For most practical applications the complexity of the geometry prevents the use of a Cartesian co-ordinate system $\{x^a\}$. Numerical co-ordinate transformations are highly desirable in that they greatly facilitate the application of the boundary conditions and transform the physical domain in which the flow is studied into a parallelepiped computational domain $\{\xi^i\}=\{\xi^1\equiv\xi,\ \xi^2\equiv\eta,\ \xi^3\equiv\zeta\}$. The most commonly used transformation is that of Thompson *et al.*,[16] which consists of solving a set of Poisson equations. This method is used here to generate two-dimensional C-type grids in planes $x^3\equiv z=$ constant parallel to the flat plate. Such grids are stacked in the z-direction.

The partially transformed RANSEs are used in their convective form for the momentum equations. The contravariant velocity components $u^i, i=1,2,3$ along ξ, η, ζ respectively, are connected to the physical Cartesian components U^a along x^a by

$$Ju^i = b^i_a U^a. \tag{4}$$

Here and in the following the convention of summation between the same indices holds; also, indices a, b, ... are associated with the Cartesian components while indices i, j, ... are associated with the curvilinear components. J is the Jacobian of the transformation from the curvilinear co-ordinates to the Cartesian co-ordinates, which is computed as the volume in the physical space of the hexahedral element image of the corresponding unit cube of the computational space. The $\mathbf{b}^i$ are the contravariant basis vectors divided by J; they are computed as the oriented areas of the faces of the hexahedral element images of the areas of the facets of the unit cube in the computational space,

$$b^k_a = [\mathbf{b}^k]_a, \quad \text{with } \mathbf{b}^i = \frac{\partial \mathbf{R}}{\partial \xi^j} \times \frac{\partial \mathbf{R}}{\partial \xi^k}, \quad i, j, k \text{ in cyclic order,} \tag{5}$$

so that the contravariant components of the metric tensor required are $g^{ij} = J^{-2}\mathbf{b}^i \cdot \mathbf{b}^j$.

The continuity equation is

$$J^{-1} \frac{\partial}{\partial \xi^i}(Ju^i) = 0, \tag{6}$$

while the developed *convective form* of the momentum equations[15,17] is written as the compact relation

$$g^{11}\phi_{\xi\xi} + g^{22}\phi_{\eta\eta} + g^{33}\phi_{\zeta\zeta} = 2A_\phi \phi_\xi + 2B_\phi \phi_\eta + 2C_\phi \phi_\zeta + R_\phi \phi_t + S_\phi. \tag{7}$$

In (7), ϕ stands for any Cartesian velocity component $U^1 \equiv U$, $U^2 \equiv V$, $U^3 \equiv W$; the source term S_ϕ, which includes pressure gradients and eventually turbulence contributions, as well as the convective coefficients A_ϕ, B_ϕ, C_ϕ and the unsteady term R_ϕ are given in Appendix I.

3. THE NUMERICS

3.1. *Convection–diffusion discretization schemes: general form*

Coefficients of ϕ-derivatives are evaluated at the centre P of the control volume and co-ordinates are normalized as

$$\xi^* = \xi/\sqrt{g^{11}}, \qquad \eta^* = \eta/\sqrt{g^{22}}, \qquad \zeta^* = \zeta/\sqrt{g^{33}}, \tag{8}$$

so that the normalized form

$$\phi_{\xi^*\xi^*} + \phi_{\eta^*\eta^*} + \phi_{\zeta^*\zeta^*} = 2A\phi_{\xi^*} + 2B\phi_{\eta^*} + 2C\phi_{\zeta^*} + R\phi_t + (S_\phi)_\mathrm{P} \tag{9}$$

is obtained, with

$$A = (A_\phi)_\mathrm{P}/\sqrt{g^{11}_\mathrm{P}}, \qquad B = (B_\phi)_\mathrm{P}/\sqrt{g^{22}_\mathrm{P}}, \qquad C = (C_\phi)_\mathrm{P}/\sqrt{g^{33}_\mathrm{P}}, \qquad R = (R_\phi)_\mathrm{P},$$

for a parallelepipedic volume (in the computational space) whose sides are given by

$$\Delta\xi^* = h = 1/\sqrt{g^{11}}, \qquad \Delta\eta^* = k = 1/\sqrt{g^{22}}, \qquad \Delta\xi^* = l = 1/\sqrt{g^{33}}.$$

If P is the centre of the control volume, τ is the time step and the index $n-1$ refers to the known state, the discretization of (9) results in

$$\frac{\Phi^{(n)}_\mathrm{P} - \Phi^{(n-1)}_\mathrm{P}}{\tau} = \sum_{nb} C_{nb}\Phi^{(n)}_{nb} - C_\mathrm{P} g, \tag{10}$$

where Φ is the approximation to the solution ϕ of (9). The index nb refers classically to neighbouring nodes (NE, NW, SE, etc.). The values of the influence coefficients C_{nb} and C_P depend on the discretization of hybrid type used for the momentum equation and are therefore omitted. From now on, $*$-symbols appearing in (9) are discarded.

3.2. Discretization based on exponential schemes

3.2.1. One-dimensional model. Instead of treating the advection and diffusion terms separately an advection–diffusion operator can be written as a single expression using the classical locally analytic solution of the linearized problem:[18]

$$\phi_{\xi\xi}-2A\phi_{\xi}=(C_U\Phi_{i-1}-\Phi_i+C_D\Phi_{i+1})/C_P=S, \tag{11a}$$

where Φ_i is the approximation of the solution ϕ of the differential equation at node x_i and

$$C_U=e^A/(e^A+e^{-A}), \qquad C_D=e^{-A}/(e^A+e^{-A}), \qquad C_P=(\tanh A)/2A. \tag{11b}$$

The coefficients of the exponential scheme are always positive. It is second-order-accurate when the cell Reynolds number A is small and it behaves as an upwind scheme when convection dominates. Although the accuracy is similar to that of the hybrid scheme, this scheme is preferred since the coefficients resulting from this discretization vary smoothly, a factor which is favourable for convergence. The scheme (11) has been extended to multidimensional cases which are presented in the following.

3.2.2. Multi-exponential (ME) scheme. The normalized transport equation can be split as follows:[14]

$$(\phi_{\xi\xi}-2A\phi_{\xi})+(\phi_{\eta\eta}-2B\phi_{\eta})+(\phi_{\zeta\zeta}-2C\phi_{\zeta})=S_{\phi}. \tag{12}$$

Each split one-dimensional advection–diffusion operator can be expressed by the exponential scheme (11).

3.2.3. Uni-exponential (UE) scheme.[14] In spite of the use of an exponential discretization, the ME scheme is found to be too diffusive. In order to decrease the numerical diffusion, a skew upwind scheme is preferred using the exponential discretization. The idea is briefly outlined below for the two-dimensional (ξ, η) case. The normalized transport equation can be written as

$$[\phi_{ss}-2\sqrt{(A^2+B^2)}\phi_s]+(\phi_{\xi\xi}+\phi_{\eta\eta}-\phi_{ss})=S_{\phi}, \tag{13}$$

where s is the local advection direction. The first term can be expressed by the exponential discretization while other second derivatives are expressed by centred differences. A parabolic interpolation function (Figure 1) is used to express the intermediate values Φ_U and Φ_D in terms of dependent variables; for instance,

$$\Phi_U=\Phi_{NW}\frac{\eta_U(\eta_U+k)}{2k^2}-\Phi_W\frac{(\eta_U+k)(\eta_U-k)}{k^2}+\Phi_{SW}\frac{\eta_U(\eta_U-k)}{2k^2}, \tag{14}$$

which results in a nine point formula. Extension to the 3D case is straightforward and a 27-point formula is obtained. Despite the fact that the 3D UE scheme is not a positive scheme, no serious difficulties have been encountered on the grid used.

3.2.4. Uni-exponential blended (UEb) scheme. The major drawback of the UE scheme is that the variation of the source term S_{ϕ} is not taken into account. Since a centred difference scheme usually gives a good approximation, it can be combined with the UE scheme to improve the

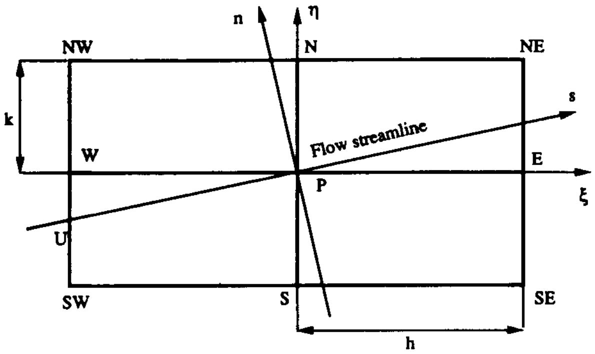

Figure 1. Molecule for the uniexponential scheme (two-dimensional example)

accuracy. The normalized transport equation is written as

$$[\phi_{ss}-2(1-\alpha)\surd(A^2+B^2)\phi_s]+\phi_{\xi\xi}+\phi_{\eta\eta}-\phi_{ss}-2\alpha\surd(A^2+B^2)\phi_s=S_\phi, \tag{15}$$

where α is a blending coefficient. All terms, except the first one which is expressed by the exponential scheme, are discretized using centred differences. Their use may introduce oscillations in the numerical solution. However, preliminary tests have shown that the best results are obtained with a blending coefficient $\alpha\approx 0{\cdot}6$.

3.3. The coupling problem and the pressure equation

In this work, following Reference 14, the well known (one-step) 'PISO' procedure[19] is used systematically. The main role of the coupling algorithm is to find an updated velocity field u^i satisfying the discrete continuity equation resulting from (6):

$$[Ju^1]_d-[Ju^1]_u+[Ju^2]_n-[Ju^2]_s+[Ju^3]_e-[Ju^3]_w=0. \tag{16}$$

At the same time the discretized momentum equation (see (10)) can be written as

$$U^a=\hat{U}^a-Cb_a^j\frac{\partial p}{\partial\xi_j}. \tag{17}$$

A non-staggered cell centred grid is used in which the pressure the velocity unknowns share the same location (Figure 2(a)). Thus only one set of influence coefficients is used for the transport equations. In contrast, on a staggered grid, C in (17) would depend on a since it would be defined at cell faces of the mass control volume, e.g. C_1 (resp. C_2) would be defined at points d and u (resp. n and s). The use of a collocated grid therefore simplifies coding and leads to significant savings in computational time and storage.

Now the problem is (i) to reconstruct the contravariant velocity components u^i needed at the control volume interfaces to ensure continuity and (ii) to avoid the chequerboard pressure oscillations. The interest of the staggered grid approach lies in the possibility of a direct substitution of mass fluxes (obtained from the momentum equation) into the continuity equation. However, when the Cartésian velocity components are the selected dependent variables, this argument works only for Cartesian co-ordinate systems in which the directions x^a of the velocity components U^a do not differ from the directions ξ^i, $i=a$, of the curvilinear co-ordinate lines. For other co-ordinate systems the required mass fluxes u^i involve simultaneously the three Cartesian velocity components U^a, which must be interpolated when not available from the momentum

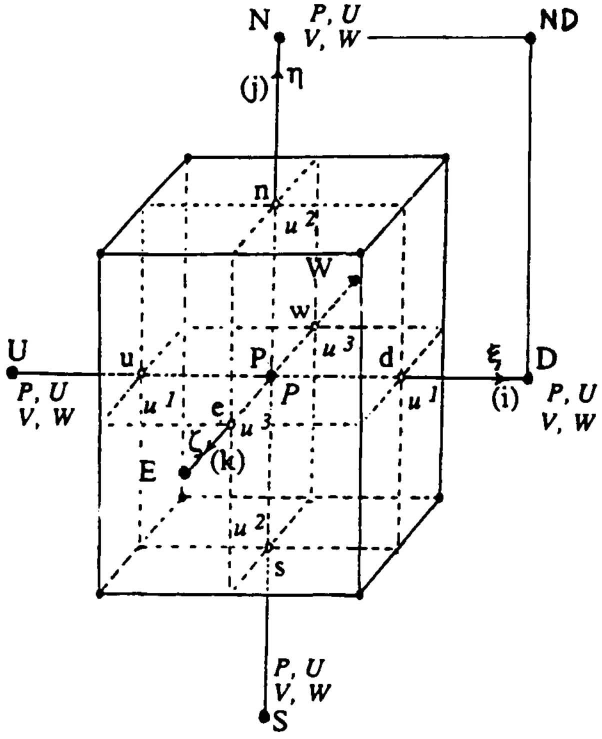

Figure 2(a). Collocated cell-centred grid. Location of the unknowns: P, U, V, W indicate the location of unknowns at points ●; U, V, W are the Cartesian velocity components; points ○ indicate the location where fluxes (or contravariant components) are needed

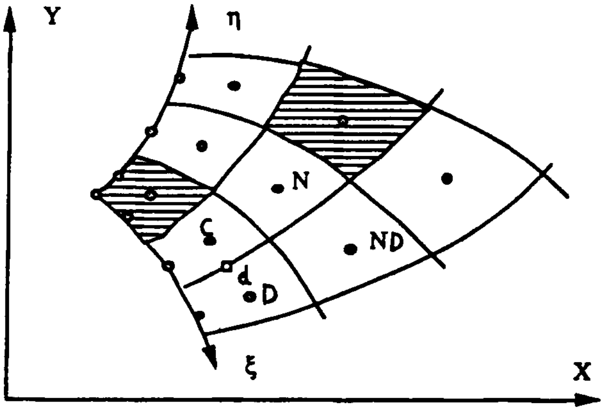

Figure 2(b). Treatment of boundary conditions; hatched areas are mass control volumes (two-dimensional sketch)

equation (i.e. when $a \neq i$). Thus the main interest of the staggered grid approach is lost on curvilinear co-ordinate systems.

Instead of building u^i from available neighbouring values, u^i is linked to other dependent variables through a local approximation of a transport equation at points d, u, . . . where fluxes are needed:

$$\bar{U}^a = \hat{U}^a - \bar{C} b_a^j \frac{\partial p}{\partial \xi^j}. \tag{18}$$

A linear interpolation $(\bar{.})$ (in the computational domain) is, however, used to build $\hat{U}^a$ and $\bar{C}$ but not the leading part of the pressure gradient at the cell interface.[20] Using relation (4), the contravariant components necessary for the continuity equation are given by

$$u^i = J^{-1} b_a^i \hat{U}^a - \bar{C} J^{-1} b_a^i b_a^j \frac{\partial p}{\partial \xi^j} \equiv J^{-1} b_a^i \hat{U}^a - \bar{C} J g^{ij} \frac{\partial p}{\partial \xi^j}, \tag{19}$$

where the fact that C does not depend on a, i.e. the collocated character of the grid, is explicitly used in the identity. Substituting the discrete form of (19) into (17) gives the discrete form of the Poisson equation:

$$\frac{\partial}{\partial \xi^i}\left(A^{ij} \frac{\partial p}{\partial \xi^j}\right) = -\operatorname{div} \hat{\mathbf{U}}. \tag{20}$$

For collocated grids the coefficients are given by $A^{ij} = \bar{C} J g^{ij}$. In contrast, $A^{ij} = \bar{C}_a J^{-1} b_a^i b_a^j$ for staggered grids (summation over a). Although A^{ij} is in both cases symmetric, the geometric factors are not required at the same points so that the pressure matrix resulting from the staggered grid approach is not symmetric. This provides a third justification for the collocated grid approach.

A significant aspect of any numerical method lies in the way boundary conditions are handled. This problem has been discussed widely in the open literature (see e.g. References 21 and 22 for a fundamental point of view). Following References 14 and 23, the control volume vertices are taken as the grid nodes while additional nodal unknowns are introduced on the boundary faces (Figure 2(b)). Although discrete molecules for the transport equations may be irregular close to the boundary, while locations for the interpolated variables may be far from the barycentre of cell centres, in the vicinity of topological singularities, this choice appears satisfactory.

The most critical issue is the pressure condition over a boundary where the velocity field is specified. If the grid is orthogonal away from the boundary, pressure boundary unknowns do not enter the pressure equation since only the contravariant velocity component is calculated on each face of a control volume when building the pressure equation. Pressure derivatives evaluated at each cell face sum to the normal pressure gradient which drives the contravariant velocity component. For instance, close to the boundary $\xi^2 = \xi_b^2$ the velocity at point d is along $\partial \mathbf{R}/\partial \xi^1$ so that $[\mathbf{grad}\, p]^1$ does not involve points in the direction $\partial \mathbf{R}/\partial \xi^2$. If the grid is non-orthogonal away from the boundary, the following approximation is used:

$$\left.\frac{\partial p}{\partial \xi^2}\right|_{\mathrm{d}} \approx \frac{P_{\mathrm{N}} + P_{\mathrm{ND}} - P_{\mathrm{C}} - P_{\mathrm{D}}}{2}. \tag{21}$$

For the present problems the grid is orthogonal close to the far-field boundary so that (21) has no influence. At the wall the grid is clustered so much that the one-side approximation (21) appears accurate enough. Moreover, although the grid is not orthogonal, (21) has a weak influence since $\partial p/\partial \xi^2$ is multiplied by g^{12}, which remains small.

The reliability of the global method is strongly dependent on the way the pressure equation is handled since the pressure solver controls the global convergence of the method. In the present method all the fluxes are used to build a three-dimensional general pressure equation. The pressure solver is therefore based on a 19-point molecule. An alternative SLOR method is applied for the solution of the resulting algebraic problem. The main interest of this approach is that the pressure matrix is symmetric and usually diagonally dominant. SLOR methods can therefore be expected to converge.

4. RESULTS

4.1. The test problem

Apart from classical benchmark cases which are presented elsewhere,[14] the validation procedure has been focused on a test geometry which consists of a hybrid profile of chord $\mathscr{C}=25{\cdot}9$ cm and thickness $\mathscr{T}=6{\cdot}1$ cm, composed of a 3:2 elliptical nose and a NACA 0020 tail joined at the location ($0.18\mathscr{C}$) of maximum thickness and mounted perpendicularly between two flat plates. The chord Reynolds number is 500 000. The wing is immersed in a fully turbulent boundary layer of momentum Reynolds number 15 000. A two-dimensional C-type grid (Figure 3) is stacked in the vertical z-direction to get the three-dimensional grid: 80 grid points are located along the chord direction ξ (55 points along the wing), while 45 points are located both in the direction normal to the aerofoil and in the direction normal to the flat plate. Even if such a grid is somewhat too coarse to capture the aerofoil thin boundary layer, it is considered to be acceptable for the junction region. The solution domain is defined by $-4\leqslant x/\mathscr{C}\leqslant 5{\cdot}5$, $0\leqslant y/\mathscr{C}\leqslant 5$ and $0\leqslant z/\mathscr{C}\leqslant 2$, the aerofoil being from zero to $\mathscr{C}$. Standard flat plate mean velocity profiles are imposed at the $\eta=\eta_{\max}$ inlet part of the outer C-shape boundary. Parabolic conditions are imposed at the downstream boundary. Plane-of-symmetry conditions are imposed at the far-field boundary $y=y_{\max}$ as well as at the symmetry planes $y=0$ and $z=z_{\max}$. Solutions are obtained down to the solid surfaces using no-slip conditions. Starting from a zero pressure field, converged results are obtained on the 162 000-point grid in about 300 iterations, which lower down the residuals by three orders of magnitude in about 90 min CPU time on the VP200 supercomputer.

4.2. Two-dimensional situation

The turbulent boundary layer thickness on the flat plate is about $0{\cdot}25\mathscr{C}$ and experiments[1] show that the influence of the flat plate can be neglected for $z>0{\cdot}5\mathscr{C}$, where the flow becomes two-dimensional. It is interesting to study this area of low viscous–inviscid interaction in order to investigate grid effects and the possible capture of the aerofoil boundary layer.

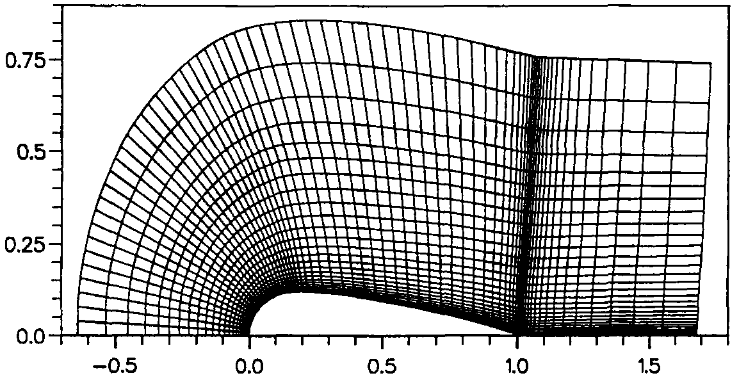

Figure 3. Two-dimensional C-type grid in a plane $z=$ constant

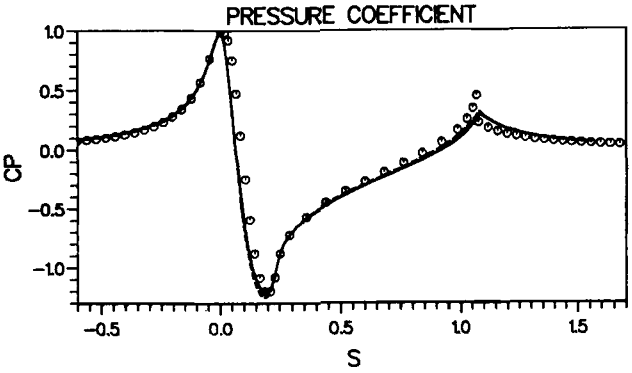

Figure 4. Evolution of the computed static pressure coefficient along the symmetry axis of the aerofoil and along its wall: O, potential flow computation; ———, ME scheme; ----, UE scheme; — — —, UEb scheme. Grid 80 × 45

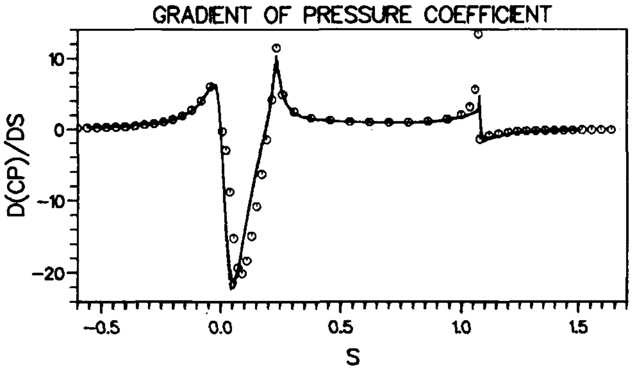

Figure 5. Evolution of the streamwise pressure gradient along the symmetry axis of the aerofoil and along its wall: O, potential flow computations; ———, ME scheme; ----, UE scheme; — — —, UEb scheme. Grid 80 × 45

Figure 4 presents the evolution of the wall pressure coefficient along the symmetry axis of the aerofoil and along the wall. The quasi-uniform velocity in the approaching flow meets a local region of adverse pressure gradient due to the obstruction created by the aerofoil. This rising pressure slows the flow and diverts it around the leading edge. As the flow accelerates on each side of the aerofoil, the pressure drops to a minimum near the area of maximum thickness of the appendage. The pressure then rises again and attains a maximum close to the trailing edge as a result of stagnation conditions there. Past the foil the pressure relaxes towards its ambient value. Except close to the leading and trailing edges of the aerofoil, the discrepancy between computed viscous flow and potential flow is very small, indicating a very low level of viscous–inviscid interaction. Differences are enhanced if the surface pressure gradient is considered (Figure 5), especially close to $s=0{\cdot}1$ where the pressure gradient is most favourable. This strong discrepancy (important from the point of view of the boundary layer which is driven by this imposed pressure gradient) is due to the discontinuity in the curvature of the hybrid aerofoil shape which has been chosen in the test case in order to magnify the horseshoe vortex system.

Owing to the low level of viscous–inviscid interaction, the most difficult phenomenon to capture is the acceleration of the flow close to the leading edge: the streamwise velocity component $U_{\max}$ at the abcissa of maximum thickness of the aerofoil (1·42 times the incoming velocity) is severely underpredicted by previous calculations.[10,12,14] A 2D calculation has been performed on the same (80 × 45) grid using three different advection schemes, namely the ME, UE and UEb schemes. Although the computed pressure fields are nearly the same, the predicted values of $U_{\max}$ are $1{\cdot}30U_0$, $1{\cdot}34U_0$ and $1{\cdot}38U_0$ respectively (Figure 6(a)). The predicted value resulting from a 2D potential flow calculation is $1{\cdot}41U_0$. Refining the grid to 110 × 80 points with the UEb scheme indicates that the Navier–Stokes solution is close to the potential solution in this section and that it slightly underestimates the experiments: the velocity overshoot is $1{\cdot}405U_0$, very close to the potential solution which agrees with experiments (Figure 6(b)).

Further downstream, computed U-velocity profiles are presented for the two mentioned grids in (Figure 7). On the fine grid the boundary layer thickness δ appears to be underpredicted because of the turbulence model. In contrast, the coarse grid results indicate an overestimation of

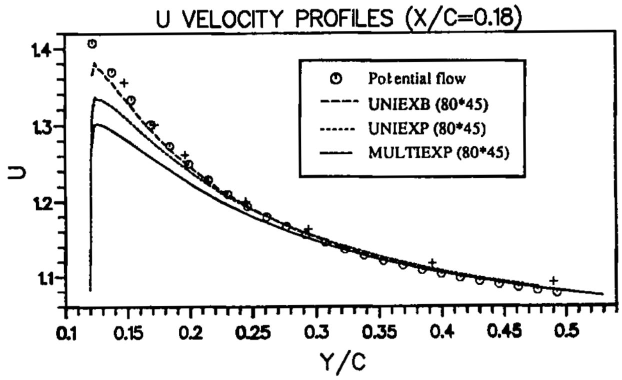

Figure 6(a). Streamwise velocity profiles U at the abcissa of maximum thickness of the aerofoil, $x/\mathscr{C}=0{\cdot}18$, with respect to the reduced normal distance $y/\mathscr{C}$ to the symmetry plane of the aerofoil: +, experiments;[1] ○, potential flow computation; ———, ME scheme; ----, UE scheme; — — —, UEb scheme. Grid 80 × 45

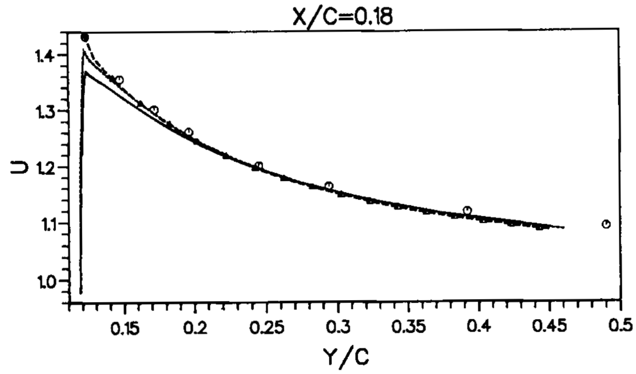

Figure 6(b). Streamwise velocity profiles U at the abcissa of maximum thickness of the aerofoil, $x/\mathscr{C}=0{\cdot}18$, with respect to the reduced normal distance $y/\mathscr{C}$ to the symmetry plane of the aerofoil: ○, experiments;[1] △, potential flow computation; ———, UEb scheme, grid 75 × 45; -----, UEb scheme, grid 110 × 80

δ associated with a high numerical diffusivity in the outer part of the boundary layer. Outside the boundary layer there is a uniform discrepancy of both potential flow and viscous flow solutions with experiments. This difference is attributed to blockage effects, as confirmed by the potential flow calculations presented in Figure 8. Taken as a whole, previous computations justify the choice of the UEb scheme for three-dimensional computations, since other tested upwind schemes do not appear so adequate in regions where the change in the pressure gradient is important.

4.3. Three-dimensional situation

The most important feature of the wing–body junction is the formation of a horseshoe vortex system in the junction region.[4,5,8,10–12,14,15] An overall picture of the flow is presented in Figure 9. Skin friction lines are visible on the flat plate and over the aerofoil as well as streamlines in the vertical symmetry plane, ahead of and behind the aerofoil. Owing to the adverse pressure gradient ahead of the aerofoil, a three-dimensional boundary layer separation results and the separation line wraps around the appendage and trails off downstream. Wall streamlines

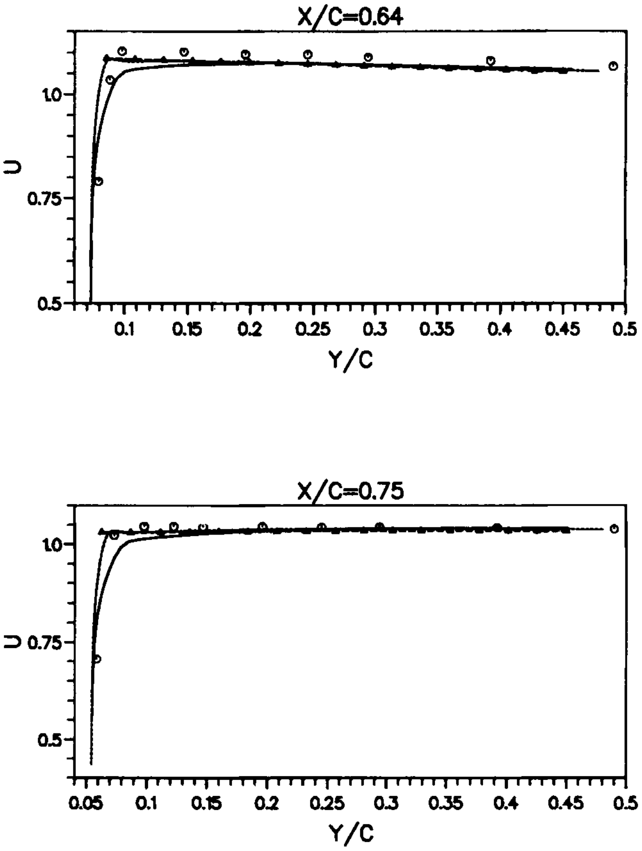

Figure 7. Streamwise velocity profiles U at $x/\mathscr{C}=0{\cdot}64$, $0{\cdot}75$, $0{\cdot}93$ and $1{\cdot}05$ with respect to the reduced normal distance $y/\mathscr{C}$ to the symmetry plane of the aerofoil: ○, experiments;[1] △, potential flow computation; ———, UEb scheme, grid 75 × 45; ----, UEb scheme, grid 110 × 80

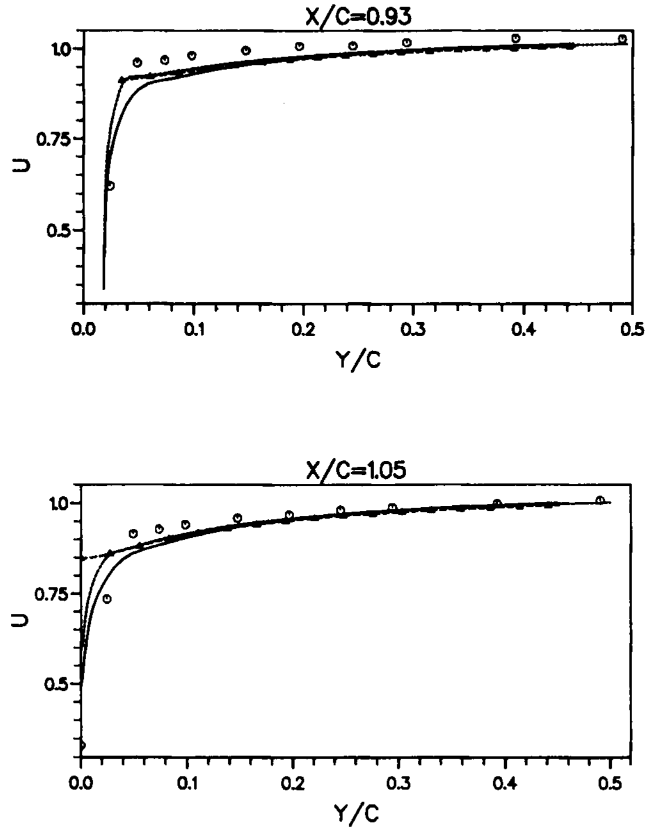

Figure 7. (Continued)

converge from both sides towards this separation line, whose origin on the plate is a saddle point S ahead of the aerofoil in its plane of symmetry. A horseshoe vortex or a system of horseshoe vortices is generated in the leading edge region of the aerofoil, each leg having vorticity of opposite rotational sense and being located between the aerofoil and a surface issuing from the separation line. A secondary root vortex can be seen close to the root of the aerofoil; it leads to a small separated trailing edge zone Σ also reported in References 10, 12 and 15.

Figures 10(a) and 10(b) focus on the skin friction pattern over the flat plate. A comparison with oil flow visualizations is presented. The primary upstream saddle point S, located at $0{\cdot}11\mathscr{C}$ (Reference 1) or $0{\cdot}47\mathscr{T}$ (Reference 2) from the wing surface (Figure 10(a)), is found in good agreement with experiments[1] as well as the 'fishtail' streamline divergence F in the wake resulting from the sudden release of the spanwise component of the surface shear stress at the wing trailing edge. This allows the two longitudinal vortices to propel fluid towards the body with consequent divergence near the body surface. Also, the divergent line located close to the aerofoil indicates the existence of a counter-rotating root vortex. A similar pattern is visible from the visualization[2] in Figure 10(b). Apart from the primary saddle point, it is seen that accumulation of pigments builds up a line formed closer to the wing than S and that this line crosses, at M, the vertical plane of symmetry only $0{\cdot}28\mathscr{T}$ upstream of the wing. This line is considered in References 1 and 2 as being one of low streamwise shear which would divide the separated flow area into a strip of high surface shear stresses, possibly generated by the time-averaged action of the horseshoe vortex, and a crescent-shaped region of apparently lower shear stress upstream. Figure 11 presents the computed isofriction levels and demonstrates that the explanation given in References 1 and 2 is wrong. Figure 10(b) indicates a more plausible explanation of the phenomenon. This line corresponds to the crest line of maximum vertical velocity W, as indicated by the isovalues of W.

Figure 12(a) confirms the correct capture of the horseshoe system in the front (vertical) plane of symmetry of the wing. The primary horseshoe vortex is centred near $x/\mathcal{C} = -0{\cdot}049$, $y/\mathcal{C} = 0{\cdot}008$, closer to the flat plate than in experiments,[2] which give $x/\mathcal{C} = -0{\cdot}047$, $y/\mathcal{C} = 0{\cdot}011$. Also, a magnified view of the root region (Figure 12(b)) indicates two embedded root vortices. Although not visible in the experiments,[1] the larger of the two is reported in Reference 2 and its size, $0{\cdot}025\mathcal{T}$, in the vertical direction also appears correctly predicted. However, the low-frequency periodic motion indicated by experiments[2] (Figure 12(c)) cannot be captured owing to the 'naive' turbulence model used and the local time-stepping procedure.

The calculated mean static pressure coefficient on the flat plate is compared with experimental data in Figure 13. Because the uncertainty in C_p is between 2% and 3% (owing to the difficulty of assigning an equivalent reference pressure and to the intrinsic measurement uncertainties), it is

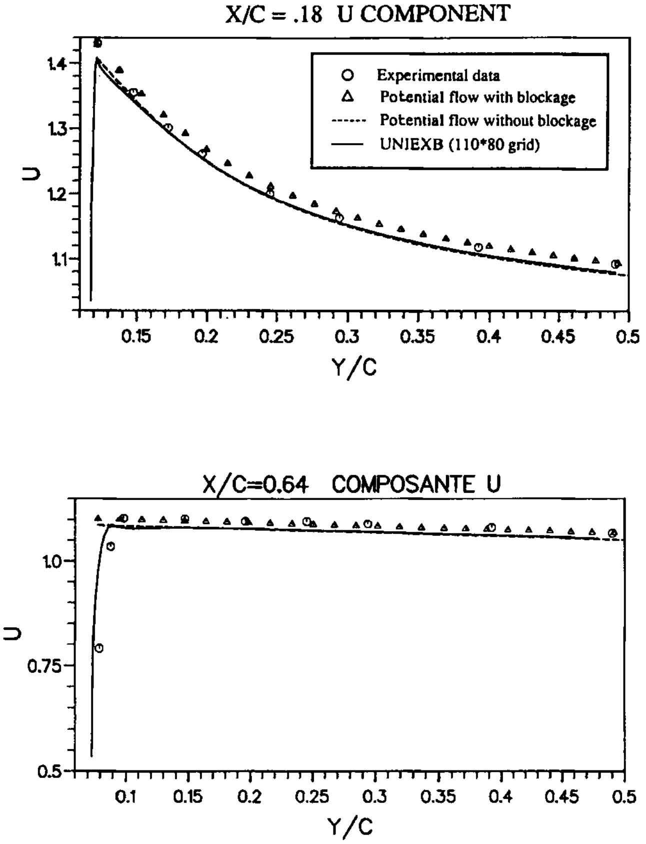

Figure 8. Influence of blockage on the streamwise velocity profiles U at $x/\mathcal{C} = 0{\cdot}18$, $0{\cdot}64$, $0{\cdot}75$, $0{\cdot}93$, $1{\cdot}05$ and $1{\cdot}50$ with respect to the reduced normal distance $y/\mathcal{C}$ to the symmetry plane of the aerofoil: ○, experiments;[1] △, potential flow computation with blockage; — — —, potential flow computation without blockage; ———, UEb scheme, grid 110×80

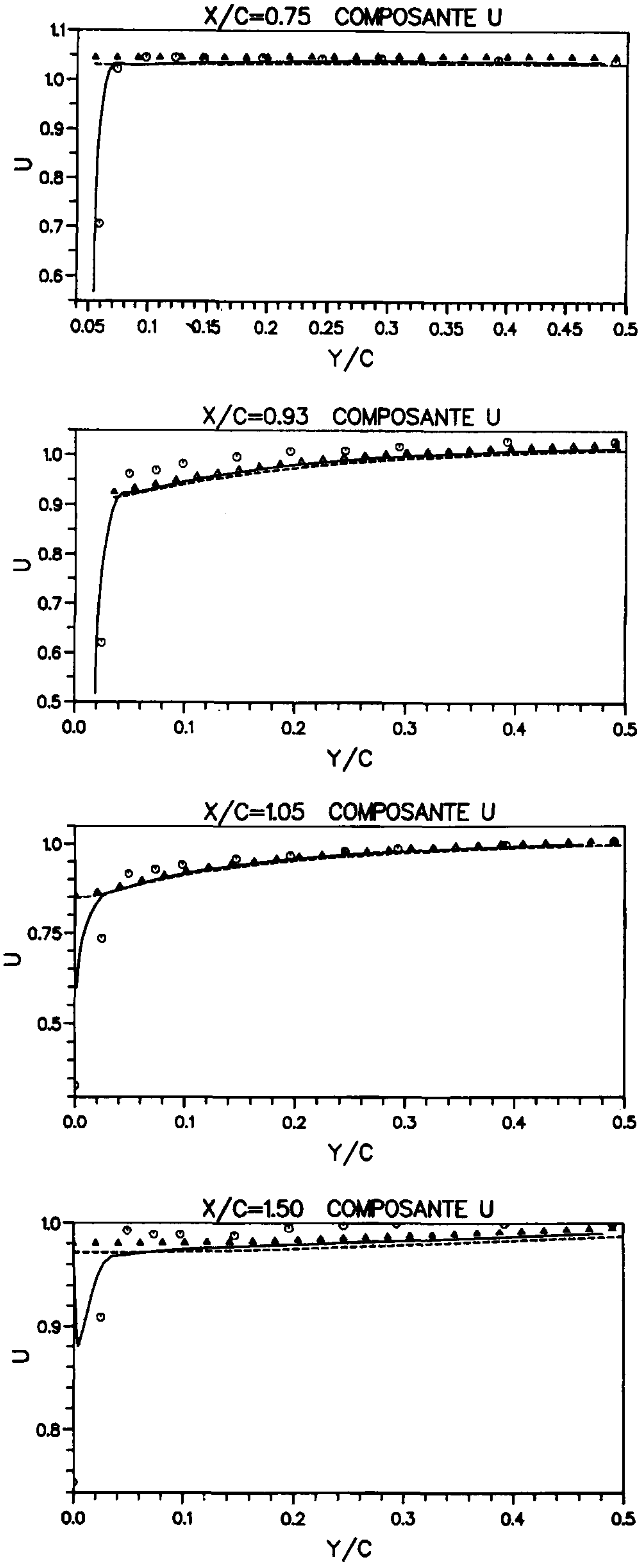

Figure 8. (Continued)

considered that the overall agreement is correct. The magnitude of C_p decreases with the distance to the flat plate, the isopressures being distorted about $0{\cdot}3\mathcal{T}$ away from the wing surface near its leading edge. This is due to the lowering of the pressure in the vicinity of the junction horseshoe vortex. This is confirmed in Figure 14, which gives the pressure coefficient as a function of the normal distance from the aerofoil. With increasing distance to the wing, the pressure first increases to a local maximum value close to the divergent line, then drops to a local minimum

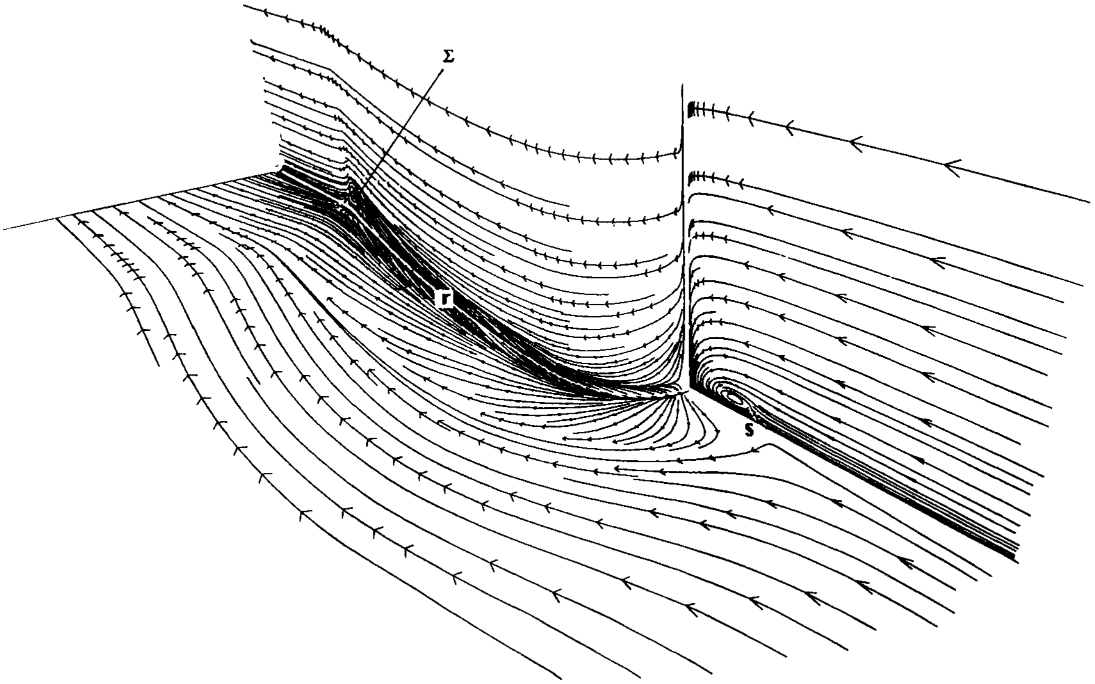

Figure 9. Overall picture of the boundary flow, in the vertical symmetry plane of the aerofoil, on the flat plate and on the aerofoil surface. S is the saddle point, Σ is the trailing edge separated zone and r is the secondary root vortex. UEb scheme, grid 80 × 45 × 45

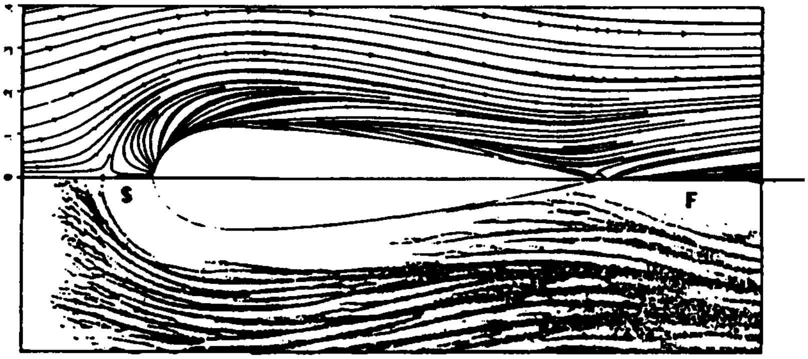

Figure 10(a). Skin friction pattern on the flat plate: upper part, computations; lower part, oil flow visualization of Reference 1. S is the saddle point and F is the fishtail streamline divergence. UEb scheme, grid 80 × 45 × 45

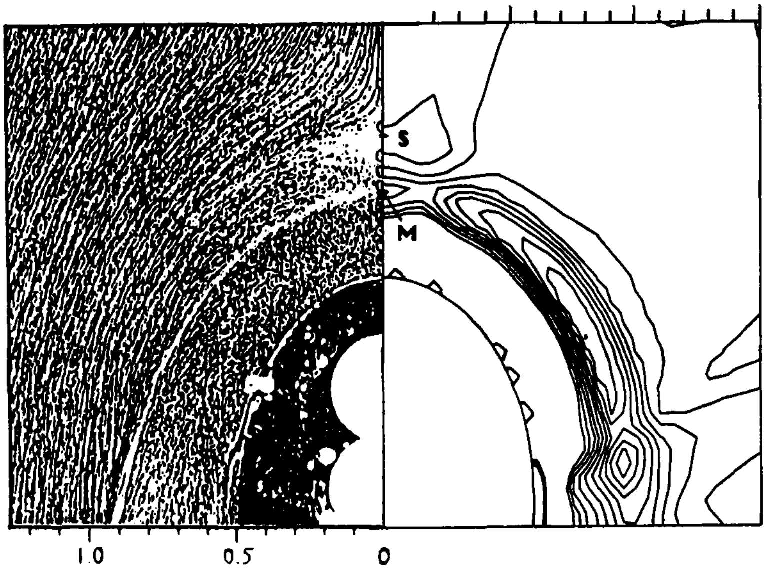

Figure 10(b).Skin friction pattern on the flat plate: left, flow visualization of Reference 2; right, isovalues of the vertical velocity component W. S is the saddle point and M is the origin of the crest line of W-values. UEb scheme, grid 80 × 45 × 45

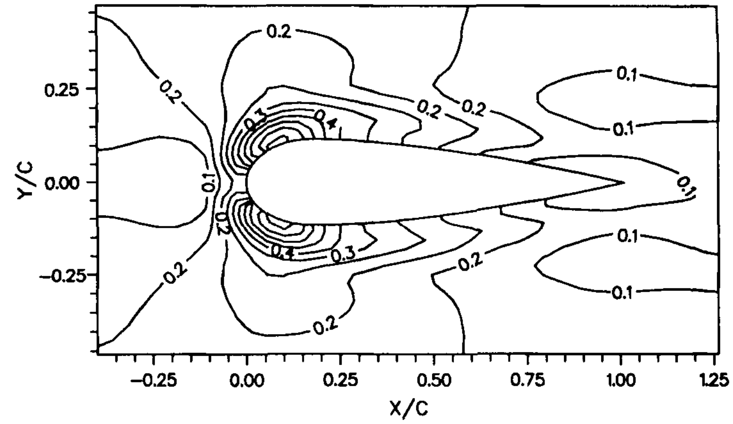

Figure 11. Computed isolevels of the skin friction coefficient. The given values are those of $100C_f$. UEb scheme, grid 80 × 45 × 45

value near the primary vortex centre, rises again to a local maximum near the separation line and finally decreases to the far-field value. Similar trends have been observed in experiments[24] and are one of the most important characteristics of viscous–inviscid interaction.

The most difficult aspect of numerical comparisons always lies in the restitution of velocity profiles. Trilinear interpolations were obviously required to make such comparisons. We first consider the aerofoil boundary layer. Computed streamwise velocity profiles as functions of $y/\mathscr{C}$ are compared with experiments[1] for several cross-sections $x/\mathscr{C}$ = constant in Figure 15. For each cross-section, velocity profiles are available for several depths $z/\mathscr{C}=\text{constant}$. The comparisons indicate that discrepancies are significant close to the flat plate, especially at $x/\mathscr{C}=0{\cdot}18$ where the aerofoil thickness is maximum. Further away from the flat plate the agreement improves. Further downstream at $x/\mathscr{C}=0{\cdot}75$ and 1·5 in the wake the same trends can be observed; however, the discrepancy is lower. Analogous results can be found in References 8 and 12, where similar comparisons are presented. Isovelocity contours are presented in Figure 16 at sections $x/\mathscr{C}=0{\cdot}18$ and 0·64. Although the main features of the flow are correctly predicted, the underestimation of streamwise velocities is confirmed, with the result that the boundary layer thicknesses are overestimated on the flat plate and, more seriously, along the aerofoil. Similar comparisons are performed in Reference 8. The present results are only marginally better at $x/\mathscr{C}=0{\cdot}18$, but the improvement obtained further downstream is qualitatively significant: the shapes of the computed isolevels between 0·7 and 0·8 are similar to the experimental isolevels here, though the values do not fit. Such shapes, which are characteristic of the influence of the horseshoe vortex, are not visible in Reference 8. Also, isolevels of 1·0 and above given here are omitted in Reference 8.

Taken as a whole, the present results share in common with results obtained by other authors' serious underestimations of the streamwise velocity profiles and overestimations of the boundary layer thicknesses. There are several reasons for such a discrepancy. The most probable is the fact

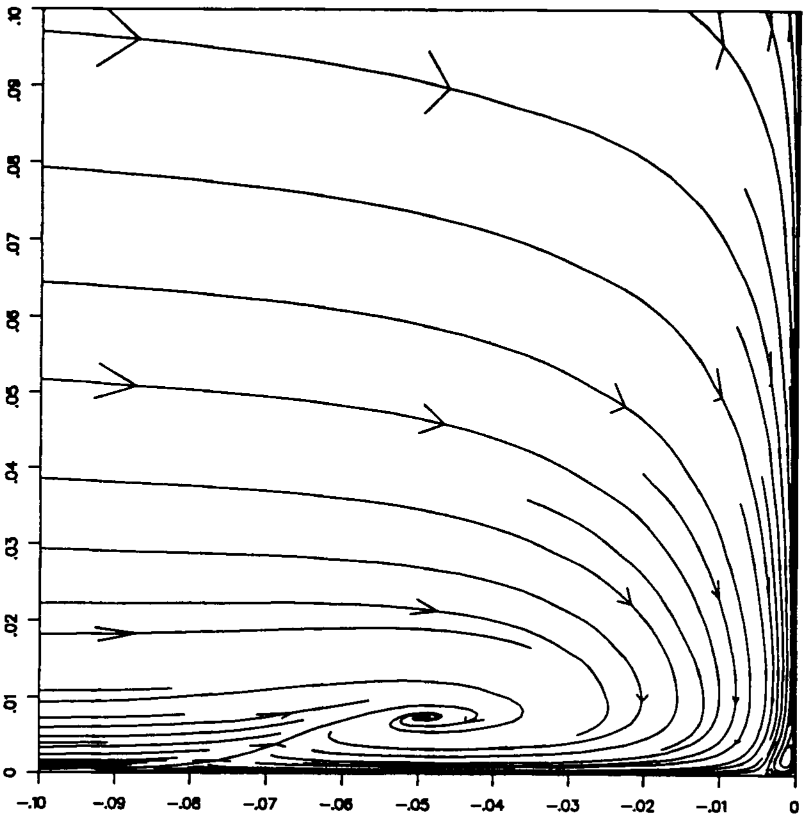

Figure 12(a). Global view of the horseshoe vortex system in the upstream symmetry plane of the aerofoil. Indicated abcissa values $x/\mathscr{C}$, ordinate values $y/\mathscr{C}$. UEb scheme, grid $80\times45\times45$

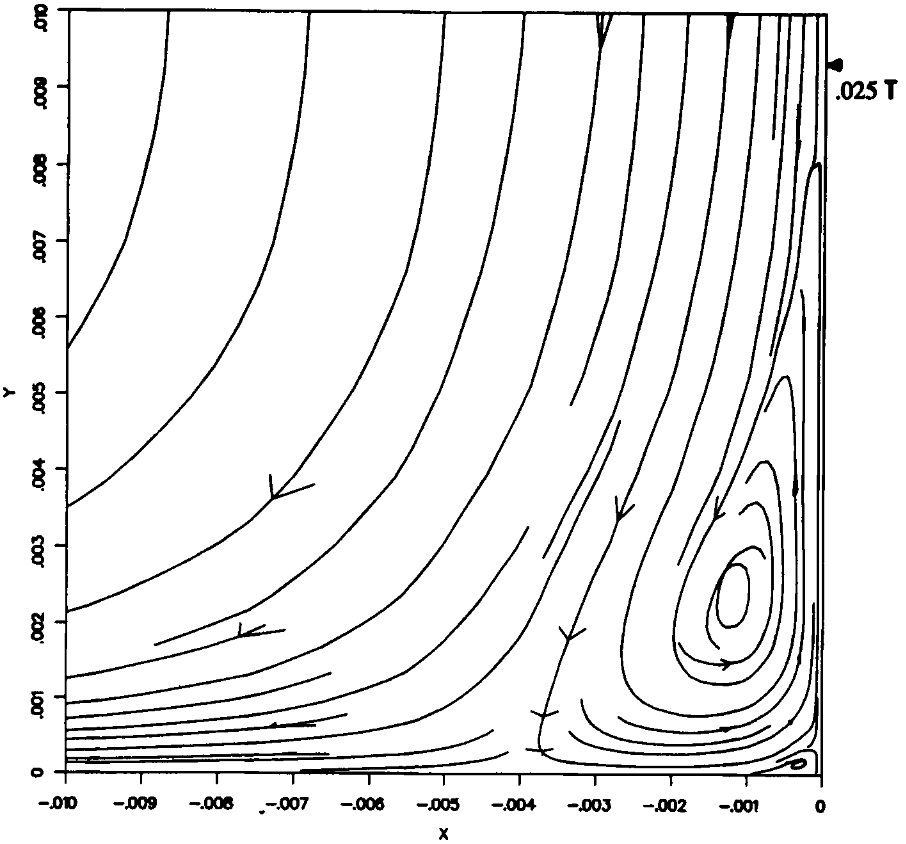

Figure 12(b). Magnified view of the embedded root vortices. Indicated abcissa values $x/\mathscr{C}$, ordinate values $y/\mathscr{C}$. UEb scheme, grid 80 × 45 × 45

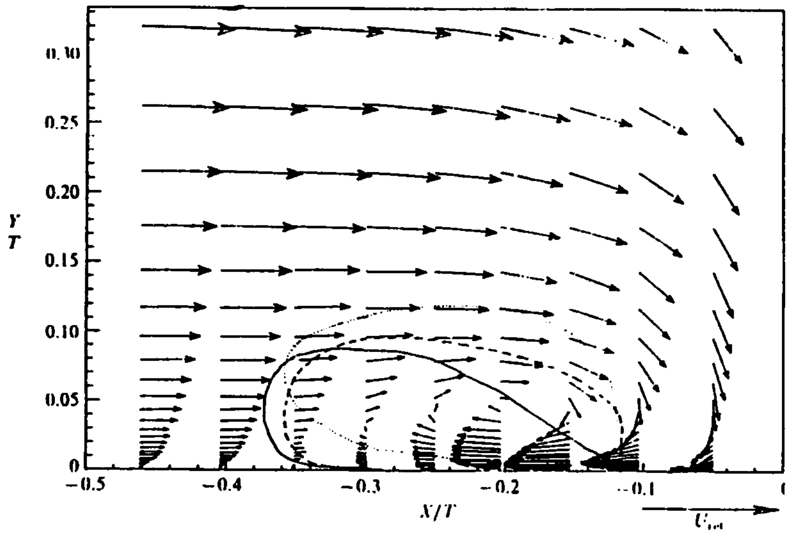

Figure 12(c). Time mean velocity vectors in the plane of symmetry. Solid, dashed and dotted lines show bimodal regions for the U-, V- and $(U - V)$-component velocity histograms respectively (taken from Reference 2)

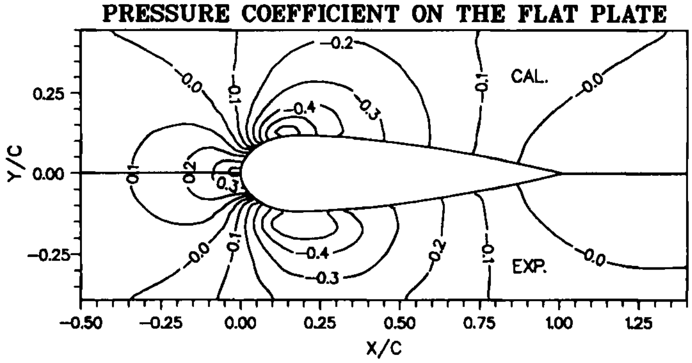

Figure 13. Mean static pressure coefficient on the flat plate: upper part, computations with the UEb scheme on an 80 × 45 × 45 grid; lower part, experimental data.

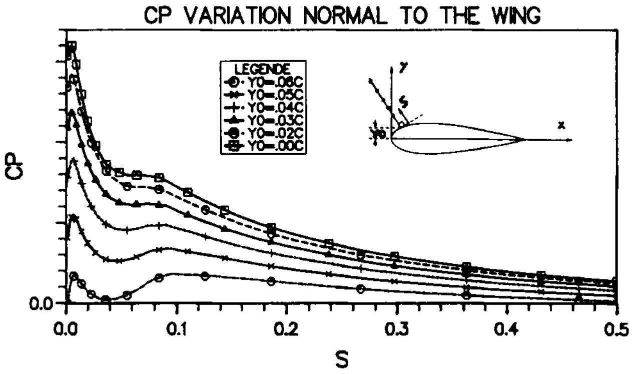

Figure 14. Variations in the pressure coefficient as a function of the normal distance to the wall taken from a point close to the leading edge at a distance YO from the symmetry plane (see legend)

that the grid is too coarse away from the aerofoil, although the need for high resolution in a thickened viscous zone is weaker than for the thin boundary layer case of low interaction considered in Section 4.2; this is confirmed by the fact that the grids used are roughly the same in References 8, 10 and 12 and here. Also, the slightly underestimated pressure peak for the lowest values of $y/\mathscr{C}$ due to blockage effects is fully consistent with measured higher velocities. Another possible reason is that no attempt has been made to explicitly model transition on the foil or to take into account the trip-wire used in the experiments. Finally, deficiencies of turbulence modelling might also partly explain the discrepancies.

5. CONCLUSIONS

A general, fully elliptic numerical method for the solution of the RANSEs has been developed and applied to wing–body junction flow. The method uses a system of numerically generated curvilinear co-ordinates and retains the Cartesian velocity components as dependent variables, a non-staggered grid, a segregated approach in which an SLOR-type pressure solver couples

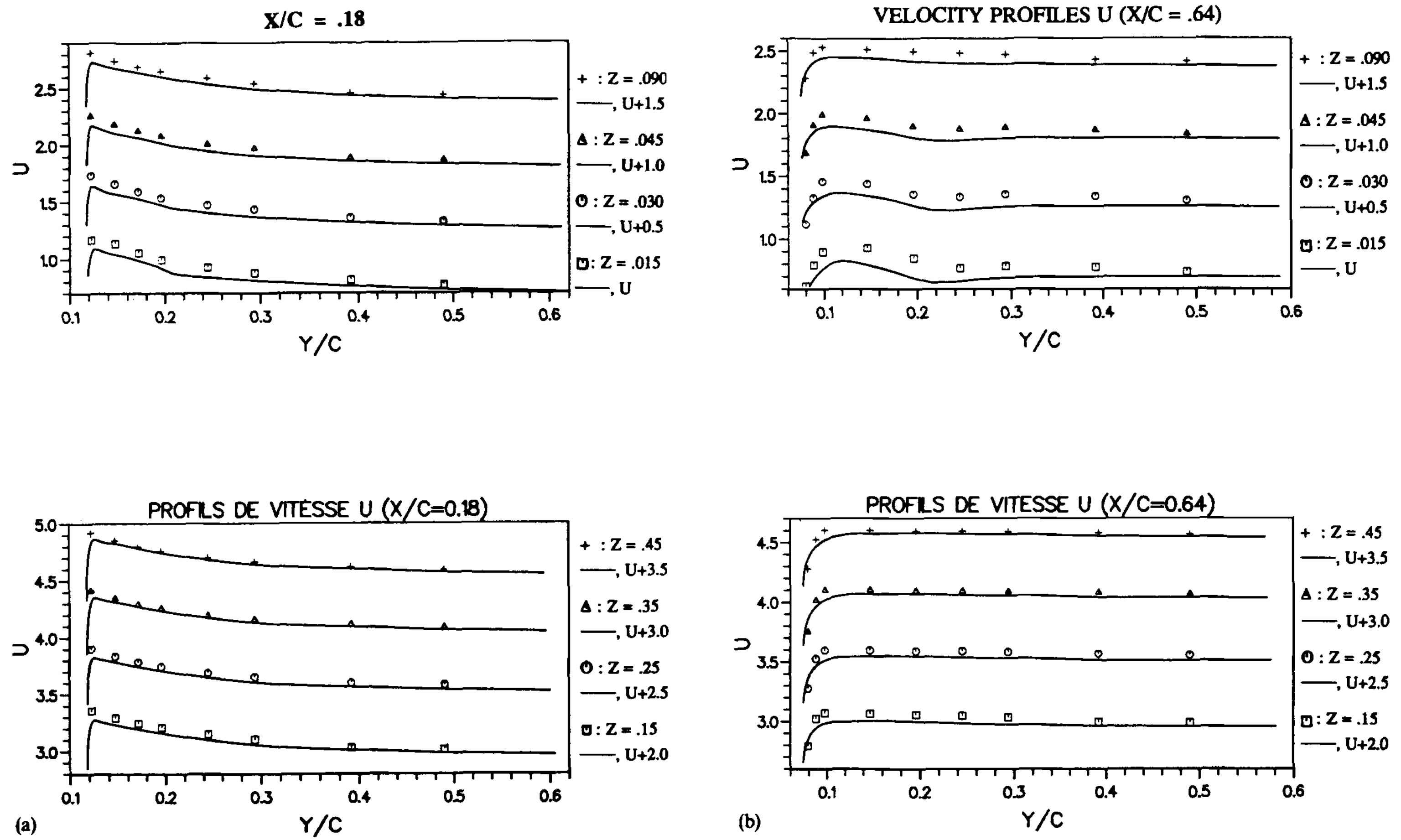

Figure 15. Streamwise velocity profiles at several cross-sections $x/\mathscr{C}$ = constant of the aerofoil. U given as a function of $y/\mathscr{C}$ for several depths $Z \equiv z/\mathscr{C}$ = constant. Computations with the UEb scheme on an $80 \times 45 \times 45$ grid

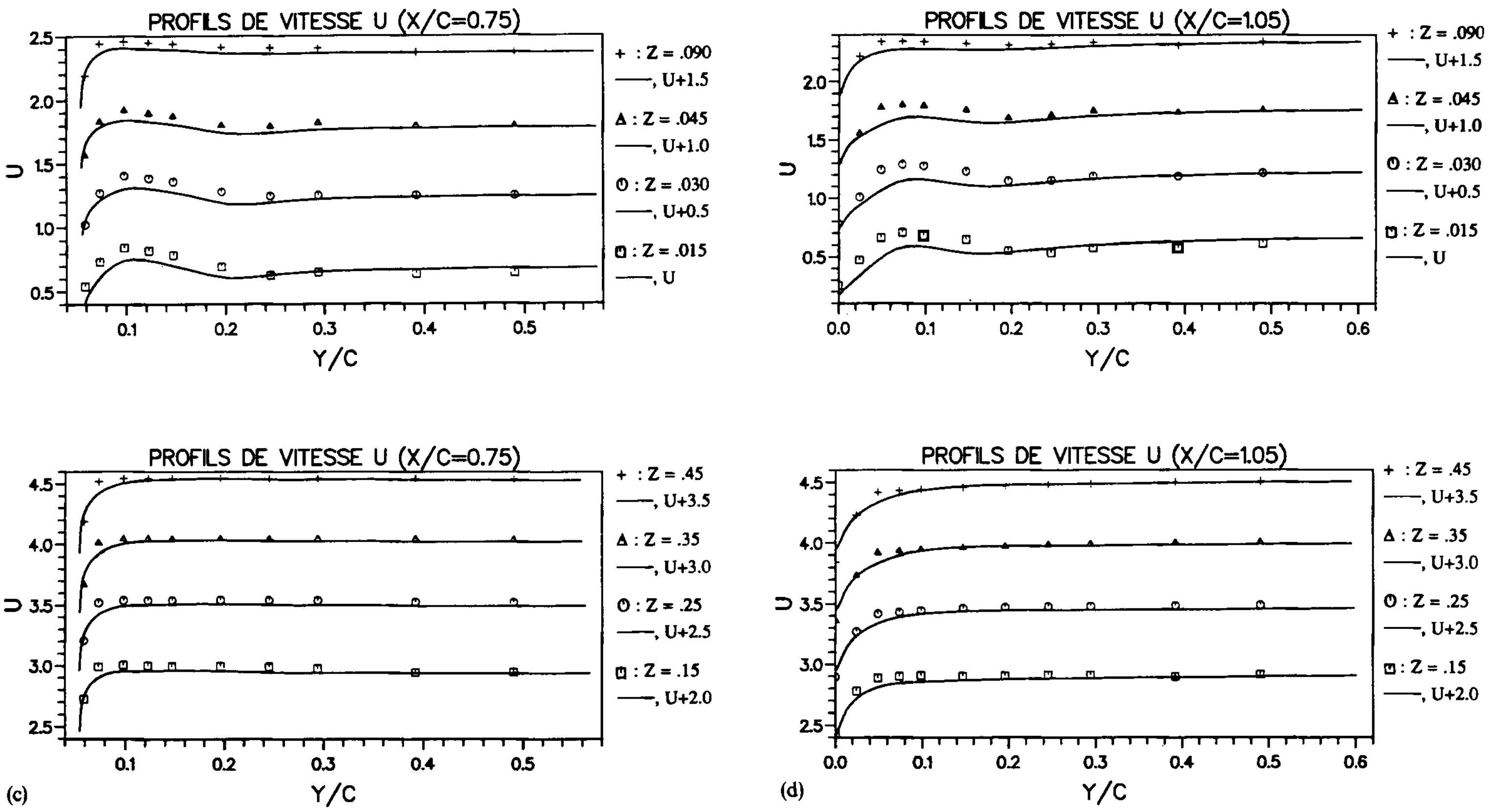

(c)

(d)

Figure 15. (Continued)

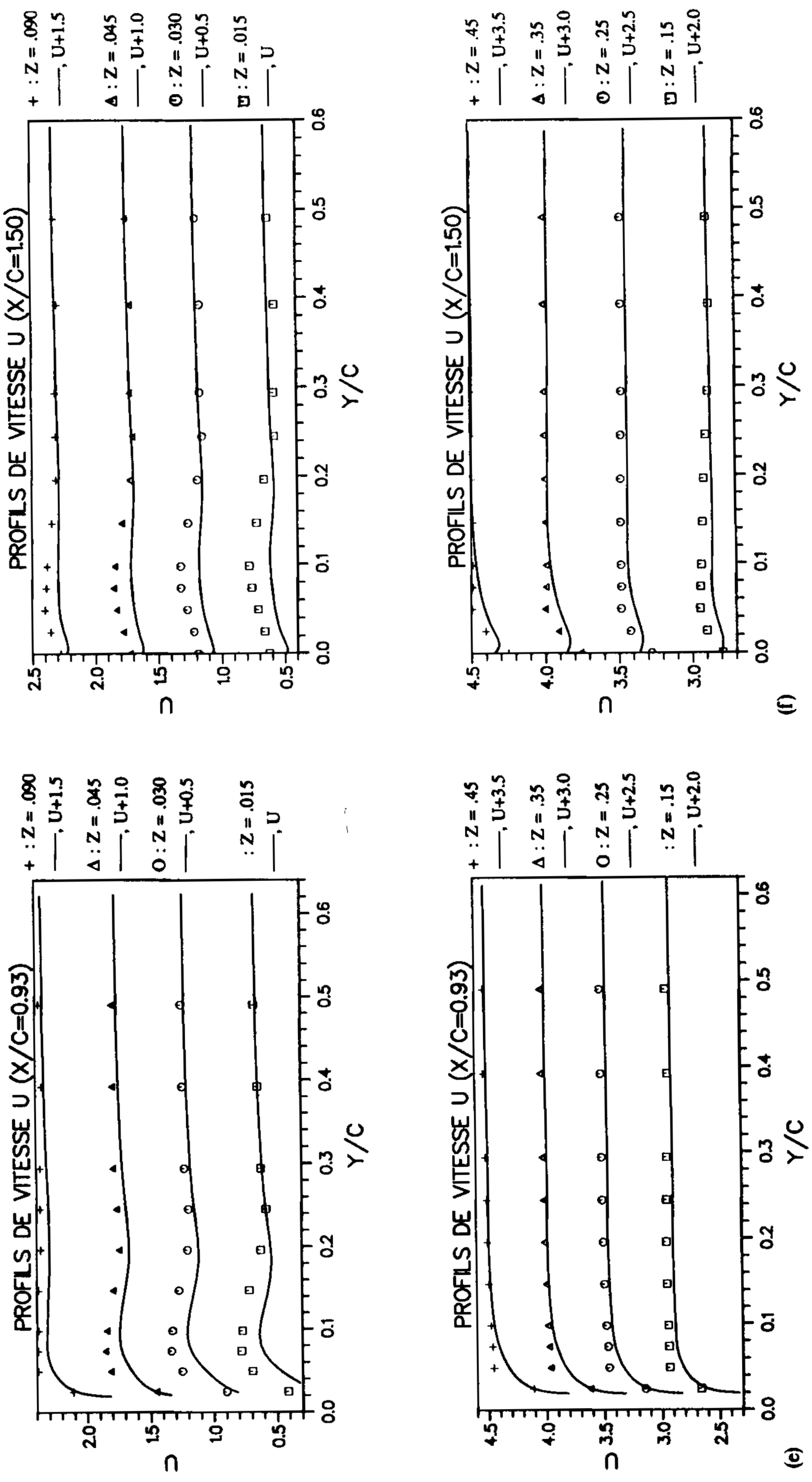

(e)

(f)

Figure 15. (Continued)

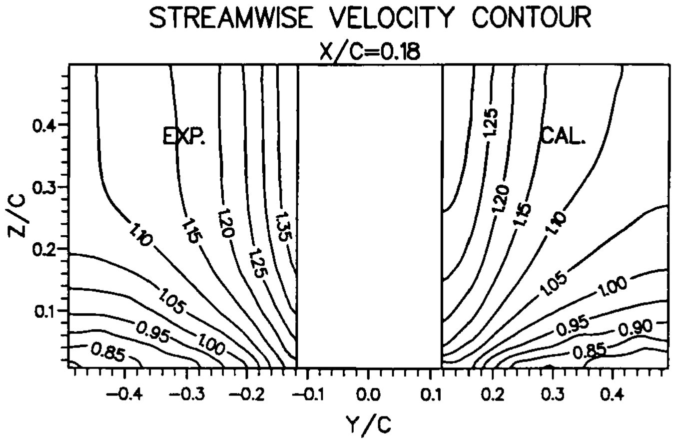

Figure 16(a). Streamwise isovelocity contours at $x/\mathscr{C}=0{\cdot}18$: left, experiments;[1] right, computations with the UEb scheme on an 80 × 45 × 45 grid. Isolevels are specified

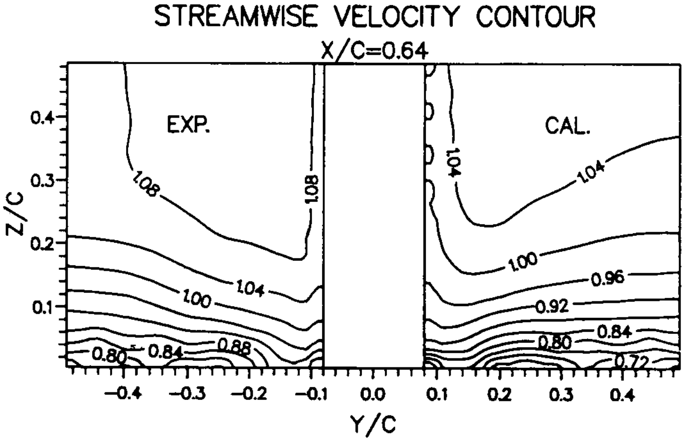

Figure 16(b). Streamwise isovelocity contours at $x/\mathscr{C}=0{\cdot}64$: left, experiments;[1] right, computations with the UEb scheme on an 80 × 45 × 45 grid. Isolevels are specified

velocity and pressure fields, and a local time-stepping method. The following conclusions emerge from this study.

With respect to *the modelling of flow characteristics*, the main features of the flow are captured. In particular, the viscous–inviscid interaction gives rise to a pressure field which looks in good agreement with experiments. The main characteristics of the horseshoe vortex system, including the location of its centre, the size of the secondary root vortex and the existence of a small trailing edge root separation, appear fully captured and a plausible explanation is given for the interpretation of oil flow patterns. The description of the mean velocity flow field in the thin boundary layers can be also considered as correct insofar as enough points are available in the region concerned. However, the omissions of blockage effects and of the transition model are believed to be responsible for most of the departure between computed and measured velocity profiles. Also, the lack of resolution in the transverse horizontal direction does not allow correct capture of the thin foil boundary layer.

With respect to *the numerical methodology*, it is felt that improvements could result from one of the following three points.

(i) *The convergence problems.* The pressure solver is the most time-consuming part of the method (about 50%). Also, the segregated PISO approach needs to be so severely underrelaxed in the first iterations that it cannot be considered as a fully reliable and robust procedure. Evidently, still more work is needed on these convergence difficulties, especially in connection with improved convection–diffusion schemes.

(ii) *The grid problems.* The optimization of the location of grid points over the flow domain cannot be considered as fully satisfactory. While the stretching control functions account here only for the friction, the description of the outer part of the boundary layer is considered to be slightly too coarse.

(iii) *The physical models.* Although the flow is mainly pressure-controlled, improvements in the turbulence models might lead at least to improved length scales. However, it is considered that an unbiased judgement over turbulence models will be conditioned by significant progress on the two aforementioned points.

ACKNOWLEDGEMENTS

Partial financial support of DRET through contracts 86-104 and 89-117 is gratefully acknowledged. Thanks are also due to the Scientific Committee of CCVR and the DS/SPI for attributions of CPU on the Cray 2 and on the VP200.

APPENDIX I

A_ϕ, B_ϕ, C_ϕ, R_ϕ and S_ϕ in (7) are given by

$$2A_\phi=\frac{R_{\mathrm{eff}}}{J}(b_j^1\alpha_\phi^j)-f^1, \qquad 2B_\phi=\frac{R_{\mathrm{eff}}}{J}(b_j^2\alpha_\phi^j)-f^2, \qquad 2C_\phi=\frac{R_{\mathrm{eff}}}{J}(b_j^3\alpha_\phi^j)-f^3,$$

$$R_\phi=a_\phi R_{\mathrm{eff}}, \qquad S_\phi=s_\phi-2(g^{12}\phi_{\xi\eta}+g^{13}\phi_{\xi\zeta}+g^{23}\phi_{\eta\zeta}). \tag{22}$$

Summation over j is omitted and the involved coefficients α, a, b, c and d are given by

$$\alpha_\phi^1=a_\phi U-\frac{b_\phi}{J}(b_1^1\nu_{\mathrm{T},\xi}+b_1^2\nu_{\mathrm{T},\eta}+b_1^3\nu_{\mathrm{T},\zeta}), \quad \alpha_\phi^2=a_\phi V-\frac{c_\phi}{J}(b_2^1\nu_{\mathrm{T},\xi}+b_2^2\nu_{\mathrm{T},\eta}+b_2^3\nu_{\mathrm{T},\zeta}),$$

$$\alpha_\phi^3=a_\phi W-\frac{d_\phi}{J}(b_3^1\nu_{\mathrm{T},\xi}+b_3^2\nu_{\mathrm{T},\eta}+b_3^3\nu_{\mathrm{T},\zeta}),$$

$$a_U=c_U=d_U=1, \quad b_U=2, \qquad a_V=b_V=d_V=1, \quad c_V=2, \qquad a_W=b_W=c_W=1, \quad d_W=2. \tag{23}$$

The additional source terms contain classically the pressure gradients and eventually the turbulence contributions. For instance, for the U-momentum equation

$$\begin{aligned} s_U=R_{\mathrm{eff}}\Bigg[&\frac{1}{J}(b_1^1p_\xi+b_1^2p_\eta+b_1^3p_\zeta)-\frac{1}{J}(b_2^1\nu_{\mathrm{T},\xi}+b_2^2\nu_{\mathrm{T},\eta}+b_2^3\nu_{\mathrm{T},\zeta})\left(\frac{1}{J}(b_1^1V_\xi+b_1^2V_\eta+b_1^3V_\zeta)\right)\\ &-\frac{1}{J}(b_3^1\nu_{\mathrm{T},\xi}+b_3^2\nu_{\mathrm{T},\eta}+b_3^3\nu_{\mathrm{T},\zeta})\left(\frac{1}{J}(b_1^1W_\xi+b_1^2W_\eta+b_1^3W_\zeta)\right)\Bigg]. \end{aligned} \tag{24}$$

It is seen that the convective form needs the functions f^i, which can be seen as purely geometrical coefficients or defined as stretching functions

$$f^i=\frac{1}{J}\frac{\partial(Jg^{ij})}{\partial\xi^j}. \tag{25}$$

APPENDIX II: NOMENCLATURE

A, B, C	local convective coefficients (see (7))
$\mathscr{C}$	aerofoil chord
C_p	pressure coefficient, $-(p-p_\infty)/0{\cdot}5\rho U_\infty^2$
g^{ij}	metric tensor of curvilinear co-ordinate system
J	Jacobian, $\mathrm{D}(x, y, z)/\mathrm{D}(\xi, \eta, \zeta)$
p	pressure
s	local curvilinear abcissa along wall streamline
s_ϕ	source term in generic equation (7)
S_ϕ	source term in (9) with crossed second-order ϕ-derivatives
$\mathbf{b}^i$	element area vector (see (5))
$\mathbf{U}$	velocity vector
U^j	contravariant velocity (ξ, η, ζ) components
U, V, W	physical Cartesian velocity components
$\overline{\mathbf{uu}}$	Reynolds stress
Re	Reynolds number
R_{eff}	effective Reynolds number, $(Re^{-1}+\nu_{\mathrm{T}})^{-1}$
$\mathscr{T}$	aerofoil thickness
ϕ	generic momentum variable
τ	time step
n	as exponent: actual discrete time
U, D, P	as indices: upstream, downstream, central points
NE, NW, etc.	as indices: cardinal points in current central ξ-station

REFERENCES

1. S. C. Dickinson, 'An experimental investigation of appendage–flat plate junction flow, Vols 1 and 2', *Rep. DTNSRDC-86/051*, 1986.
2. W. J. Devenport and R. L. Simpson, 'Time-dependent and time-averaged turbulence structure near the nose of a wing–body junction', *J. Fluid Mech.*, **210**, 23–55 (1990).
3. I. M. M. A. Shabaka and P. Bradshaw, 'Turbulent-flow measurements in an idealized wing–body junction', *AIAA J.*, **19**, 131–132 (1981).
4. W. R. Briley and H. McDonald, 'Computation of threedimensional horseshoe vortex flow using the Navier–Stokes equations', *Proc. 7th ICNMFD*, Stanford, CA, W. C. Reynolds and R. W. MacCormack (Eds.) *Lect. Notes Phys.*, **141**, Springer, 1981, pp. 91–98.
5. R. C. Buggeln, R. B. Briley and H. McDonald, 'Solution of the three-dimensional Navier–Stokes equations for a turbulent horseshoe vortex flow', *Final Rep. AD-A176 370*, SRA, Glastonbury, CT, 1987.
6. B. S. Baldwin and H. Lomax, 'Thin-layer approximation and algebraic model for separated turbulent flows', *AIAA Paper 78-257*, 1978.
7. J. J. Gorski, T. R. Govindan and B. Lakshminarayana, 'Comparison of threedimensional turbulent shear flows in corners', *AIAA J.*, **23**, 685–692 (1985).
8. R. W. Burke, 'Computation of turbulent incompressible wing–body junction flow', *AIAA Paper 89-0279*, 1989.
9. D. Kwak, J. L. C. Chang, S. P. Shanks and S. R. Chakravarthy, 'A threedimensional incompressible Navier–Stokes flow solver using primitive variables', *AIAA J.*, **24**, 390–396 (1986).
10. C. H. Sung and C. I. Yang, 'Validation of turbulent horseshoe vortex flows', *Proc 17th Symp. on Naval Hydrodynamics*, Den Haag, National Acad. Press, Washington D.C., 1989, pp. 241–256.
11. C. H. Sung and M. J. Griffin, 'Improvements in incompressible juncture flow calculations', *AIAA Preprint*, 1991.

12. H. C. Chen and V. C. Patel, 'The flow around wing–body junctions', *Proc. 4th Symp. on Numerical and Physical Aspects of Aerodynamic Flow*, T. Cebeci, (Ed.) California State Univ., Long Beach, CA, 1989, Session 3.1.
13. M. Wolfshtein, 'The velocity and temperature distribution in one-dimensional flow with turbulence augmentation and pressure gradient', *Int. J. Heat Mass Transfer*, **12**, 301–318 (1969).
14. G. B. Deng, 'Résolution des equations de Navier–Stokes tridimensionnelles, application au calcul d'un raccord plaque plane–aile', *Ph.D. Thesis*, University of Nantes, 1989.
15. G. B. Deng, J. Piquet, P. Queutey and M. Visonneau, 'Three-dimensional full Navier–Stokes solvers for incompressible flows past arbitrary geometries', *Int. j. numer. methods eng.*, **31**, 1427–1451 (1991).
16. J. E. Thompson, Z. U. A. Warsi and C. W. Mastin, *Numerical Grid Generation, Foundations and Applications*, North-Holland, New York, 1985.
17. H. C. Chen, V. C. Patel and S. Ju, 'Solutions of the Reynolds-averaged Navier–Stokes equations for three-dimensional incompressible flows', *J. Comput. Phys.*, **88**, 305–336 (1990).
18. D. B. Spalding, 'A Novel finite difference formulation for differential equations involving both first and second order derivatives', *Int. j. numer. methods eng.*, **4**, 551–559 (1972).
19. R. I. Issa, 'Solution of the implicitly discretised fluid flow equations by operator-splitting', *J. Comput. Phys.*, **62**, 40–65 (1985).
20. C. M. Rhie and W. L. Chow, 'Numerical study of the turbulent flow past an isolated airfoil with trailing edge separation', *AIAA J.*, **21**, 1525–1532 (1983).
21. P. M. Gresho and R. L. Sani, 'On pressure boundary conditions for the incompressible Navier–Stokes equations', *Int. j. numer. methods fluids*, **7**, 1111–1143 (1987).
22. P. M. Gresho, 'Incompressible fluid dynamics; some fundamental formulation issues', *Ann. Rev. Fluid Mech.*, **23**, 413–453 (1991).
23. M. Peric, 'A finite volume method for the prediction of three-dimensional fluid flow in complex ducts', *Ph.D. Thesis*, University of London, 1985.
24. S. Sarohia and A. D. Young, 'Wind tunnel investigations of some three-dimensional separated turbulent boundary layers', *IUTAM Symp. on Three-dimensional boundary Layers*, Springer, 1982, pp. 126–137.